



A Data-driven machine learning model for radiation-induced DBTT shifts in RAFM steels

Pengxin Wang ^{a,b}, G.M.A.M. El-Fallah ^{a,*}

^a School of Engineering, University of Leicester, Leicester LE1 7RH, UK

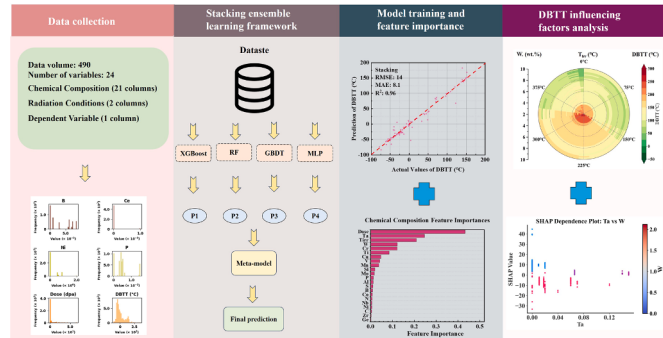
^b Nanjing Iron & Steel United Co., Ltd., Nanjing, 210035, Jiangsu, China



HIGHLIGHTS

- Built a stacking model (XGBoost, RF, GBDT, MLP) for DBTT prediction ($R^2 = 0.96$).
- Identified dose, temperature, Ta, W, and Cr as key factors for DBTT evolution.
- DBTT peaks from 150 to 300 °C and >30 dpa, then drops above 350 °C due to recovery.
- Ta and W reduce DBTT by stabilising precipitates and limiting defect growth.
- SHAP shows that W lowers DBTT via solid solution strengthening at 6–9 % Cr and 0–0.04 % Ta.

GRAPHICAL ABSTRACT



ARTICLE INFO

Keywords:

Reduced activation ferritic martensitic (RAFM) steels
ductile-to-brittle transition temperature (DBTT)
Machine learning
GBDT
XGBoost
Random forest
Artificial neural network

ABSTRACT

This study develops a stacking ensemble machine learning model to predict ductile-to-brittle transition temperature (DBTT) in irradiated Reduced-Activation Ferritic-Martensitic (RAFM) steels. Using a dataset of 490 irradiation cases, the model integrates XGBoost, Random Forest (RF), Gradient Boosting Decision Tree (GBDT), and Multi-Layer Perceptron (MLP), achieving a high predictive accuracy ($R^2 = 0.96$) and outperforming individual models. The results highlight the significant influence of irradiation dose and temperature on DBTT. Beyond 30 dpa, defect accumulation causes a sharp DBTT increase, while irradiation temperature exhibits a nonlinear effect, peaking at 150–300 °C due to radiation-enhanced precipitation and declining above 350 °C as defect recovery improves ductility. Additionally, alloying elements play a crucial role: Ta and W help mitigate embrittlement, moderate Cr (4–6 wt. %) increases DBTT, and higher Cr levels (>6 wt. %) reduce it at elevated temperatures. SHAP analysis reveals that W is particularly effective in reducing embrittlement in alloys with moderate Cr (6–9 wt. %) and low Ta, while higher Cr concentrations (>6 wt. %) help stabilise DBTT at elevated temperatures. To enable practical alloy design, a genetic algorithm was combined with the model to optimise steel compositions under defined irradiation conditions (200–350 °C, 10 dpa). The approach successfully identified candidate alloys with predicted DBTT values below 50 °C. This study provides a robust predictive framework for understanding and optimising DBTT in irradiated RAFM steels, offering valuable insights into their performance in next-generation nuclear reactors.

* Corresponding author.

E-mail address: gmae2@leicester.ac.uk (G.M.A.M. El-Fallah).

1. Introduction

Reduced-activation ferritic-martensitic (RAFM) steels, known for their excellent mechanical properties and radiation resistance, have emerged as key structural materials for future fusion reactors and advanced nuclear applications. However, radiation exposure significantly alters their mechanical behaviour, particularly the ductile-to-brittle transition temperature (DBTT), which defines the threshold temperature below which the material transitions from ductile to brittle fracture. The shift in DBTT under irradiation is a crucial factor that limits the operational reliability of RAFM steels, as it determines the lower boundary of their service temperature window [1,2]. The primary cause of DBTT elevation in RAFM steels is radiation embrittlement, which arises from microstructural modifications induced by neutron irradiation, including defect accumulation, phase transformations, and solute segregation at grain boundaries [3–6]. These radiation-induced phenomena collectively degrade the fracture toughness of RAFM steels,

increasing their susceptibility to brittle fracture and ultimately restricting their service life in nuclear environments [7].

Extensive research has been conducted to investigate the mechanisms of radiation embrittlement and its influence on DBTT shifts in RAFM steels. It has been well established that neutron irradiation generates point defects, including vacancies and self-interstitial atoms (SIAs), which subsequently aggregate to form defect clusters, dislocation loops, and voids [8–10]. These irradiation-induced defects impede dislocation motion, reducing plastic deformation capability and causing an increase in DBTT [11,12]. Additionally, radiation-induced segregation (RIS) and precipitate evolution further contribute to embrittlement [13]. RIS leads to the migration of solute elements, such as phosphorus and silicon, towards grain boundaries, weakening intergranular cohesion and promoting brittle fracture [14–16]. Concurrently, radiation-enhanced precipitation results in the formation of carbides and second-phase particles, which further obstruct dislocation movement and contribute to embrittlement [17,18]. Studies have

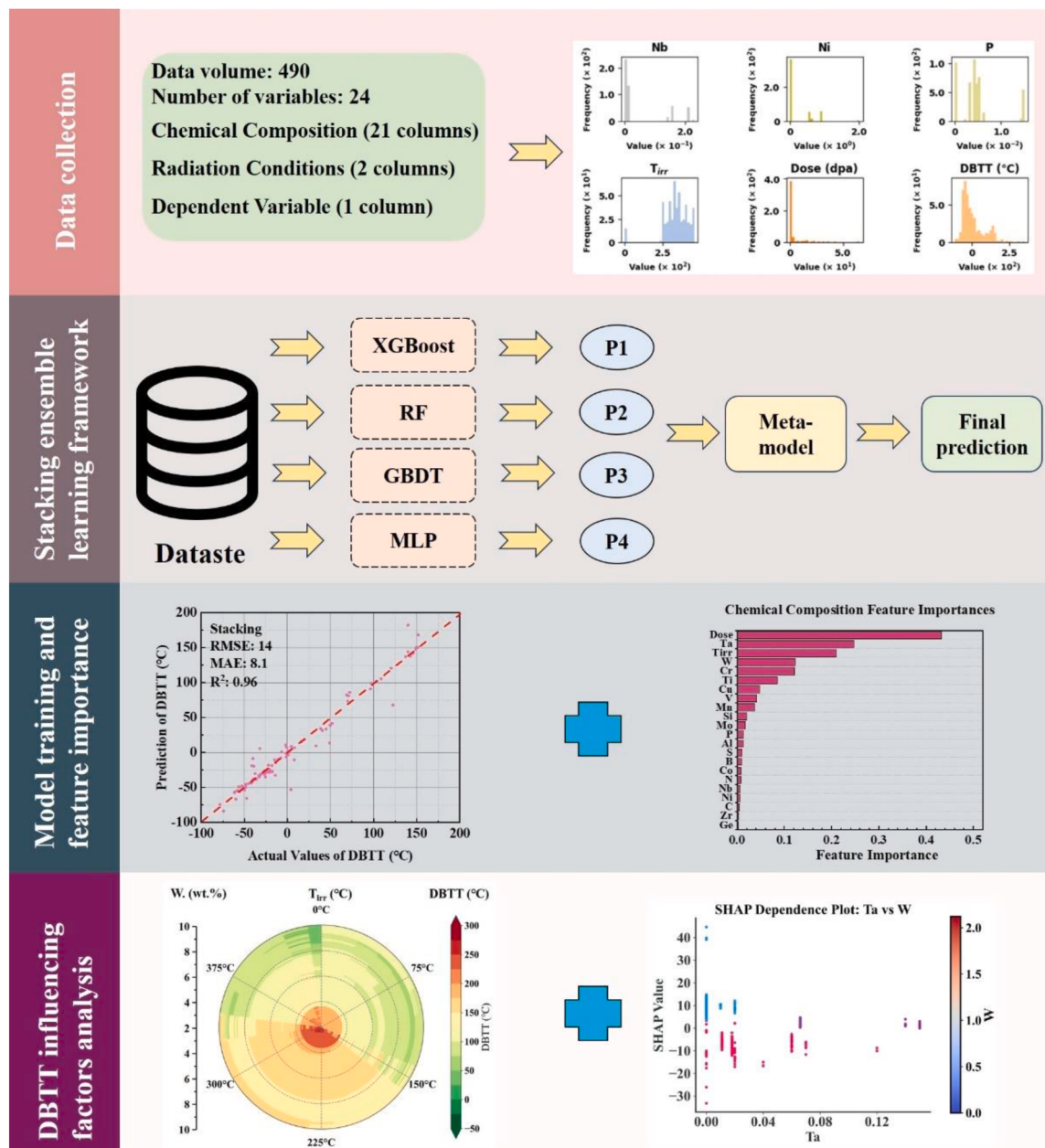


Fig. 1. Flowchart of methodology.

demonstrated that the density and thermal stability of these precipitates vary with irradiation temperature and dose, explaining the complex and nonlinear nature of DBTT shifts [19–21]. Advanced microstructural characterisation techniques, such as atom probe tomography (APT) and transmission electron microscopy (TEM), have further revealed that dislocation loop morphology changes significantly with irradiation conditions, with loop coarsening and annihilation occurring at elevated temperatures [7,22,23]. Despite these advancements, a comprehensive understanding of DBTT evolution in irradiated RAFM steels remains elusive, as multiple microstructural mechanisms interact at different length scales.

Experimental studies on DBTT shifts in irradiated RAFM steels are hindered by high costs, prolonged irradiation times, and safety constraints due to the handling of radioactive materials [24]. As a result, available experimental datasets are often sparse and limited in scope, preventing a holistic understanding of DBTT behaviour across different RAFM compositions and irradiation conditions [25]. To address these challenges, researchers have sought to develop predictive models for estimating radiation-induced DBTT-shift. Early empirical models considered microstructural features such as dislocation loop density and carbide precipitation [26,27]. However, these methods rely on experimental input parameters, such as the density and size of defects and precipitates, which are often derived from incomplete datasets, thereby restricting their predictive accuracy [28]. Moreover, these approaches typically assume homogeneous defect distributions and do not fully account for the complex interactions between atomic-scale defects and macroscopic fracture behaviour, limiting their applicability in real-world scenarios [26–28].

Machine learning (ML), a subset of artificial intelligence, has revolutionised data-driven analysis in materials science, offering predictive capabilities that are particularly valuable in cases where experimental data are scarce or highly variable. Over the past two decades, ML has been successfully applied to various challenges in materials research, including predicting fracture toughness, optimising heat treatment processes, and modelling phase transformations [29–32]. Korotaev et al., [33] used a neural network to predict irradiation swelling in austenitic steels and proposed alloy optimisation guidelines. Johnson et al., [34] used machine learning to predict defect concentrations in irradiated materials, reducing computational costs. Zhu et al., [35] developed a machine-learning framework to predict complex residual stress distributions in laser-welded Eurofer97 steel, enhancing the structural reliability of fusion reactor components.

Although ML has been increasingly employed to model irradiation-induced embrittlement phenomena, most existing studies focus on conventional reactor pressure vessel (RPV) steels, and very few have addressed DBTT shifts in RAFM steels. For example, He et al. [36] used six ML algorithms, including XGBoost and random forest, to predict ΔRT_{NDT} in commercial RPV steels, identifying Cu content and neutron fluence as dominant factors. However, their dataset excludes RAFM steels and focuses solely on ΔRT_{NDT} rather than actual DBTT. Similarly, Lee et al. [37] evaluated Cubist, support vector machine (SVM), and XGBoost models using the ASTM E900–15 database and demonstrated improved transition temperature shift (TTS) prediction accuracy. Nevertheless, their study remains confined to high-Cu steels and conventional fission reactor conditions. Xu et al. [38] proposed an XGBoost-based TTS model, but their approach does not address RAFM compositions or the high-dose irradiation relevant to fusion environments. More recently, Jacobs et al. [39] developed a neural network ensemble with uncertainty quantification to predict TTS in RPV steels, but their model was not validated for RAFM alloys. Despite the growing application of ML in embrittlement modelling, comprehensive data-driven studies explicitly addressing DBTT shifts in irradiated RAFM steels, especially under fusion-relevant dose and temperature conditions, remain scarce.

To address these limitations, this study develops a stacking ensemble model integrating XGBoost, Random Forest (RF), Gradient Boosting

Decision Tree (GBDT), and Multi-Layer Perceptron (MLP) to predict and analyse DBTT shifts in irradiated RAFM steels. Through hyperparameter optimisation, the proposed framework enhances predictive accuracy and mitigates overfitting, ensuring robust generalisation across diverse datasets. Additionally, the model is employed to systematically evaluate the influence of chemical composition and irradiation conditions on DBTT evolution, providing deeper insights into the mechanisms of radiation-induced embrittlement in RAFM steels.

2. Computational methodology

The methodology is summarised in the flowchart shown in Fig. 1. Initially, a systematic literature review was conducted to compile data related to the DBTT, forming a comprehensive dataset. As illustrated in the top section of Fig. 1, this dataset comprises 490 data points with 24 variables, carefully compiled from various academic sources spanning 1990 to 2024. It includes data on reduced-activation steels such as Eurofer97, F82H, OPTIFER, ORNL, JLF, and CLAM. The dataset contains 21 chemical composition variables, including Niobium (Nb), Nickel (Ni), Phosphorus (P), Carbon (C), Chromium (Cr), Tungsten (W), Molybdenum (Mo), Vanadium (V), Silicon (Si), Manganese (Mn), Nitrogen (N), Aluminium (Al), Arsenic (As), Boron (B), Cobalt (Co), Copper (Cu), Oxygen (O), Titanium (Ti), Zirconium (Zr), and Molybdenum (Mo). Additionally, it includes two irradiation-related parameters: Irradiation Dose (Dose) and Irradiation Temperature (Tirr), with DBTT as the dependent variable. The distributions of some key variables are displayed in the right-hand section of the data collection panel in Fig. 1. A comprehensive description of the dataset, including the data acquisition process, is provided in the supplementary material under “Data Collection and Description.”

To develop an accurate predictive model for DBTT based on the chemical compositions and radiation conditions of RAMF steels, a stacking ensemble learning framework was implemented, as shown in the second section of Fig. 1. This framework integrates multiple machine learning models, XGBoost, RF, GBDT, and MLP, each trained independently to generate preliminary predictions (P1, P2, P3, and P4). These predictions are then fed into a meta-model, which synthesises their outputs to generate the final DBTT prediction. This approach leverages the strengths of different models, enhancing predictive performance by reducing bias and variance.

Following model development, training and validation were conducted using statistical metrics, including root mean square error (RMSE), mean absolute error (MAE), and coefficient of determination (R^2). The scatter plot in the left section of the third panel in Fig. 1 presents the comparison between predicted and actual DBTT values for the stacking model. The right section of the third panel in Fig. 1 shows the feature importance analysis results. The performance comparison of the stacking model and its four base models is provided in the supplementary material under “Model Training and Selection.”

Finally, a detailed investigation into the impact of key parameters on DBTT was conducted. As depicted in the final section of Fig. 1, polar coordinate charts were employed to visualise the effects of irradiation dose and temperature, as well as chemical composition variations. Additionally, this study utilised SHAP to analyse the synergistic effects of elements. This comprehensive analysis provides valuable insights into the mechanisms governing radiation-induced embrittlement in RAMF steels, supporting material optimisation efforts. Building upon these insights, a genetic algorithm was integrated with the machine learning model to perform targeted composition optimisation under irradiation conditions. The resulting alloy candidates satisfy defined physical constraints while exhibiting low predicted DBTT values, offering a practical path towards the design of irradiation-tolerant RAFM steels. Through this structured approach, this research aims to enhance the understanding of DBTT behaviour in reduced-activation steels, offering theoretical guidance for alloy design and performance improvement.

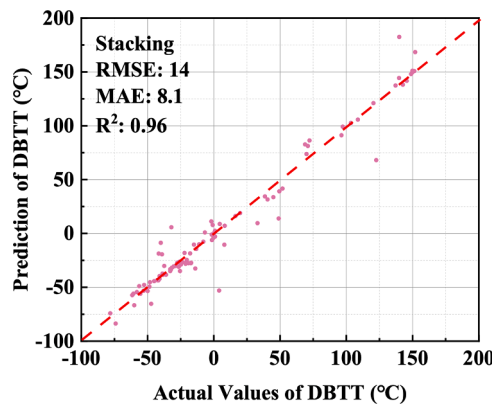


Fig. 2. Stacking model prediction performance for DBTT, indicating a high correlation with RMSE = 14 °C, MAE = 8.1 °C, and R²=0.96.

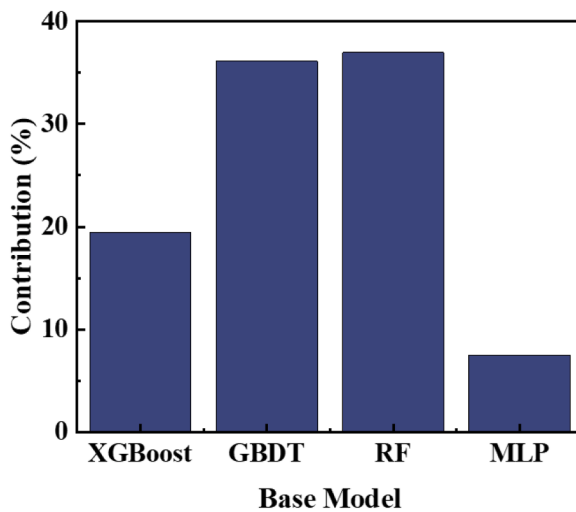


Fig. 3. Contribution of each base model to the stacking ensemble, calculated using the absolute coefficients of the Ridge final estimator. The contributions reflect the relative importance of each base learner (XGBoost, GBDT, RF, and MLP) in the overall prediction framework.

3. Results and discussion

3.1. Model training

Fig. 2 illustrates the relationship between actual and predicted DBTT values obtained using the stacking ensemble model, which combines XGBoost, RF, GBDT, and MLP as base learners. The model demonstrates high predictive accuracy, achieving RMSE = 14 °C, MAE = 8.1 °C, and R² = 0.96. The tight clustering of data points along the diagonal reference line indicates strong agreement between predicted and actual values, confirming the effectiveness of the stacking approach in capturing complex, nonlinear relationships within the dataset.

The stacking model outperforms all individual base models, exhibiting lower prediction errors and higher generalisation capability, which can be attributed to its ability to leverage the complementary strengths of multiple learners. A detailed performance comparison between the stacking model and its base components is provided in the Supplementary Material: Model Comparison.

To quantitatively evaluate the contribution of each base learner within the stacking ensemble framework, we extracted the absolute coefficients of the final estimator (Ridge regression) after model training. These coefficients were normalised and converted to percentage contributions to reflect the relative importance of each model in

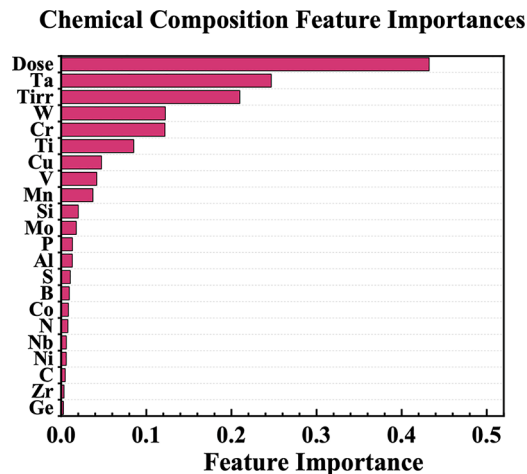


Fig. 4. Stacking model Feature Importance for DBTT, indicating radiation Dose as the most influential feature, followed by Ta, Tirr, W, and Cr.

forming the final prediction.

As shown in Fig. 3, all four base models contributed meaningfully to the overall ensemble output, confirming the effectiveness of model diversity within the stacking framework. Gradient Boosting (GBDT) and Random Forest (RF) exhibited the highest contributions, each accounting for over 30 % of the total influence. XGBoost also played a substantial role ($\approx 19\%$), while the Multi-Layer Perceptron (MLP) contributed approximately 10 %. Although the MLP model had the lowest weight, its inclusion improved ensemble performance by capturing complementary, non-tree-based representations of the data. This demonstrates that the ensemble benefits from the heterogeneity of model architectures and that the stacking approach successfully integrates information from both tree-based and neural models to enhance robustness and generalisation across complex irradiation datasets.

3.2. Feature importance analysis

To investigate the contribution of individual input features to the stacking ensemble model, a weighted feature importance analysis was performed. For the three tree-based base learners (XGBoost, GBDT, and Random Forest), feature importance was obtained directly from their built-in `feature_importances_` attribute. In contrast, the Multi-Layer Perceptron (MLP) model does not natively provide such metrics, and therefore, permutation importance was calculated based on the reduction in R² score upon random shuffling of each feature.

To integrate the results from different models, an R²-based weighting scheme was adopted. Specifically, each base learner's R² score on the test set was normalised and used as a weight to combine the feature importance vectors. This ensured that the final ensemble-level importance reflects both the internal relevance assigned by each model and its predictive strength.

The resulting ranked feature importances are shown in Fig. 4. The radiation dose is the most influential feature, followed by Ta, Tirr, W, and Cr. The high-ranking factors, Dose, Ta, Tirr, W, and Cr, will be further analysed in the Discussion section, where their impact on DBTT shift will be examined in detail.

Elements such as Ni, Cu, Al, Co, B, Nb, and Zr exhibit relatively low importance in the ranking. This is expected, as these elements are strictly limited in low-activation steels [40,41], resulting in minimal compositional variations and thus reduced influence on DBTT shifts. Additionally, C content remains around 0.1 % across all compositions, leading to consistently low variation and subsequently a lower ranking in feature importance.

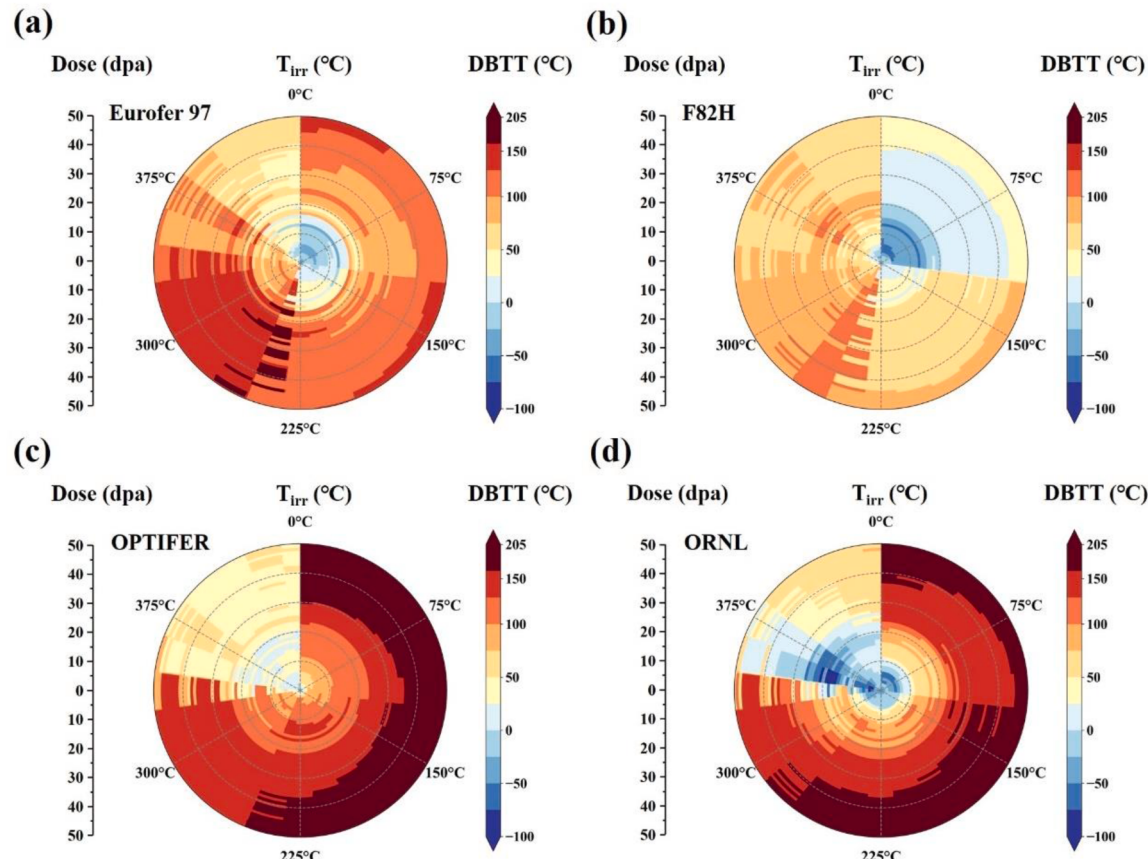


Fig. 5. Polar contour analysis of DBTT variations in four representative Reduced-Activation Ferritic-Martensitic (RAFM) steels under irradiation: (a) Eurofer 97, (b) F82H, (c) OPTIFER, and (d) ORNL. Each plot presents a visual representation of DBTT ($^{\circ}\text{C}$), where the angle corresponds to irradiation temperature ($^{\circ}\text{C}$) and the radius represents dose (dpa).

3.3. Effects of radiation temperature and dose

Based on the validation in the previous section, our model demonstrates high accuracy, enabling us to predict and analyse the effects of irradiation temperature and dose on the DBTT. To intuitively visualise the relationships between these variables, we employ polar coordinate charts, which facilitate clear observation and analysis of the impact of temperature and dose on DBTT. In these charts, temperature is represented by the angle, increasing clockwise from 0°C to 450°C ; irradiation dose (dpa) is represented by the radius, extending from the centre (0 dpa) to the edge (50 dpa); and DBTT ($^{\circ}\text{C}$) is indicated by the colour gradient, ranging from deep blue (lowest DBTT) to dark red (highest DBTT), as shown by the legend.

Fig. 5(a) presents the polar coordinate chart of Eurofer97 steel. At low doses below 10 dpa and temperatures up to 225°C , the DBTT remains low (approximately -50°C to 0°C), indicating good toughness. As the irradiation dose increases beyond 30 dpa, especially between 225°C and 300°C , the DBTT rises sharply above 100°C , signalling significant embrittlement. Above 350°C , a narrow recovery region emerges, with DBTT decreasing to 50°C , although this effect is limited to a narrow temperature band.

For F82H steel, shown in Fig. 5(b), at doses below 10 dpa and temperatures up to 225°C , the DBTT remains very low, with a pronounced deep-blue region ($<0^{\circ}\text{C}$), indicating superior resistance to embrittlement. As the dose increases beyond 30 dpa at $225\text{--}300^{\circ}\text{C}$, the DBTT

rises moderately, typically to $50\text{--}100^{\circ}\text{C}$, but does not reach the extreme values seen in Eurofer97. At higher temperatures above 350°C , the DBTT generally stabilises or slightly declines, although the recovery effect is less pronounced compared to Eurofer97.

For OPTIFER steel, shown in Fig. 5(c), the DBTT remains low at doses below 10 dpa and temperatures from 75°C to 225°C . However, compared to Eurofer97 and F82H, OPTIFER exhibits a much faster DBTT increase with rising dose and temperature. At doses exceeding 30 dpa across the 0°C – 300°C range, DBTT rises above 150°C , indicating severe embrittlement. Although there is a minor recovery trend above 350°C , the high-temperature, high-dose regions largely remain embrittled, as indicated by the persistent red zones.

For ORNL steel, shown in Fig. 5(d), the DBTT is very low ($<0^{\circ}\text{C}$) at doses below 10 dpa and temperatures up to 225°C , indicating excellent toughness. As the dose increases beyond 30 dpa and temperatures rise to 300°C , the DBTT increases, but embrittlement remains less severe compared to OPTIFER and Eurofer97. Above 300°C , a broad and clear recovery region appears, with DBTT reducing to $0\text{--}50^{\circ}\text{C}$, highlighting the material's strong thermal recovery capability over a wide temperature range.

It should be noted that the DBTT contours presented in Fig. 5 are based on predictions from a machine learning model trained on a large and diverse dataset, which includes over 400 data entries extracted from published literature and experimental reports. These data span multiple RAFM steel grades, irradiation sources, and irradiation conditions. As

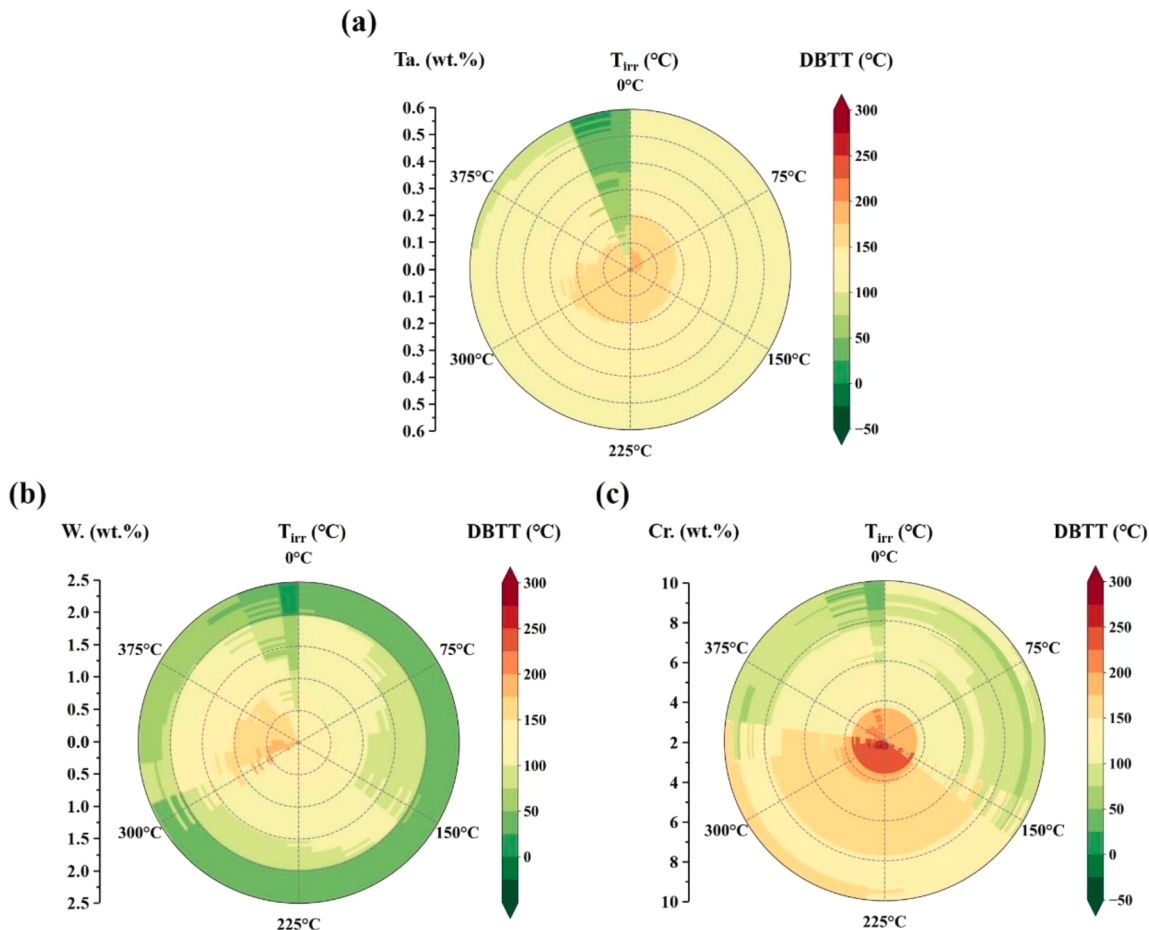


Fig. 6. Effect of alloying elements on DBTT in Eurofer97 steels across different temperatures. Each chart provides a visual representation of DBTT (°C), with radiation temperature (°C) indicated by angle and element content (wt. %) by radius.

such, the contour maps are intended to reflect overall trends in embrittlement behaviour, rather than reproducing the outcome of any individual experiment.

Although a previous study reported pronounced irradiation-induced embrittlement in F82H steels at temperatures below 300 °C and low doses [42], these results do not universally apply to all processing or irradiation conditions. Several other experiments have demonstrated that when F82H is properly tempered and irradiated under favourable microstructural conditions, the DBTT can remain below 0 °C even at temperatures around 250 to 300 °C. For example, Shiba et al., [43] observed a relatively modest increase in DBTT from -50 °C to 0 °C after irradiation at 250 to 265 °C with 0.8 dpa, and Jia and Dai [44] reported that F82H steel irradiated up to 8.6 dpa at approximately 265 °C still exhibited a DBTT below -80 °C, as measured by small punch testing. These findings highlight the substantial variability in embrittlement response, which depends not only on irradiation temperature and dose but also on steel composition, heat treatment, and initial microstructure.

Therefore, the presence of deep-blue regions in our predicted DBTT maps does not imply an absence of irradiation-induced embrittlement. Instead, these regions represent comparatively lower DBTT values relative to other conditions and other RAFM steels in the dataset. Given the statistical nature of the model, the contours reflect data-driven generalised behaviour across a wide range of material states and test

conditions, rather than providing point-by-point matches with any single experiment. The model's predictions should thus be interpreted as probabilistic trends derived from the overall dataset distribution.

Fig. 5 clearly illustrates that irradiation dose remains the predominant factor influencing the DBTT. Across all four RAFM steels, DBTT exhibits a consistent increase with rising irradiation dose, regardless of temperature. The influence of radiation dose has been extensively studied [8,10,20,45], with findings consistently highlighting its role in inducing irradiation-induced defects such as vacancy clusters, dislocation loops, helium bubbles, and micro-voids. As radiation dose increases, these defects accumulate, progressively impeding grain boundary and dislocation movement, which in turn elevates DBTT [21,46,47]. This finding aligns well with the predicted results.

In contrast, the influence of irradiation temperature varies among different steel types. For Eurofer 97 and F82H, DBTT exhibits a relatively modest increase when irradiation temperatures range between 0 °C and 225 °C. Previous research suggests that, within this temperature range, the dominant irradiation-induced defects in RAFM steels are micro-voids, gas bubbles, and small defect clusters [19,48]. At lower temperatures, these defects initially increase in number but eventually stabilise due to the limited diffusion kinetics, thereby exerting a relatively minor impact on DBTT. However, as the irradiation temperature exceeds 225 °C, defect clusters begin to grow significantly [49,50], leading to a

further increase in DBTT and material embrittlement. Additionally, studies indicate that above 225 °C, Cr atoms tend to segregate at dislocations and grain boundaries, further exacerbating DBTT elevation [16–18]. Beyond 350 °C, high-temperature exposure facilitates defect rearrangement and partial annealing recovery [51], allowing martensitic laths to undergo recovery while simultaneously reducing defect density [52]. This microstructural evolution contributes to an improvement in ductility, consequently leading to a decrease in DBTT.

3.4. Effects of element content

Based on the results of the variable importance analysis, only Ta, W, and Cr have a relative importance greater than 0.1. Therefore, this study focuses solely on investigating the effects of Ta, W, and Cr on DBTT. Similar to the previous section, polar coordinate charts are used to see the effect of element content on the radiation hardening of Eurofer97. In these charts, the temperature is represented by the angle, increasing clockwise from 0 °C to 450 °C. The element content (Ta, W, Cr) is represented by the radius, extending from the centre (0 wt. % for Ta and W, 2 wt. % for Cr) to the edge (0.6 wt. % for Ta, 2.5 wt. % for W, and 10 wt. % for Cr). The DBTT (°C) is indicated by the colour scale, ranging from deep green (lowest DBTT, improved toughness) to red (highest DBTT, severe embrittlement), with the colour legend providing specific values. The radiation dose is set to a fixed value of 35 dpa. As the above study shows, at this dose level, the degree of radiation hardening is the highest, which helps in analysing the effects of elements on radiation hardening.

Particular attention was given to the selection of elemental composition ranges in this study, based on both the composition limits typically used in RAFM steels and the need to explore potential optimisation strategies. For Ta, we extended the range up to 0.6 wt. % because it is widely recognised as a beneficial element in RAFM steels, introduced to replace Mo and enhance mechanical stability. Moreover, our feature importance analysis indicated that Ta has a relatively large contribution to the DBTT-shift, further justifying the inclusion of a broader Ta range to provide insights for alloy design. For Cr, although some early experimental studies included steels with Cr contents exceeding 10 wt. %, the compositions currently used in practical RAFM steels generally fall within the 2–10 wt. % range. Therefore, we defined the Cr range accordingly. Similarly, the W content in practical RAFM steels typically remains within the 0–2.5 wt. % range and has already been well studied in the literature, and we set the range in line with this practical context. These choices were made to ensure that the model reflects both historical data trends and practical alloy design considerations, providing meaningful guidance for future material development.

Fig. 6(a) shows a polar coordinate chart of Ta content. The results show that DBTT is generally lower at higher Ta contents, particularly at elevated irradiation temperatures, where dark green regions become more pronounced, indicating improved resistance to embrittlement. At lower irradiation temperatures and low Ta concentrations (<0.2 wt. %), DBTT remains moderately high (yellow regions), but no extreme red zones are observed, indicating that embrittlement is limited even at low Ta levels.

The contour plot reveals a relatively consistent trend across all temperature ranges, where DBTT decreases gradually with increasing Ta content, as indicated by the progressive expansion of green regions. Unlike Cr or W, which exhibit distinct temperature-dependent effects, Ta appears to provide a relatively uniform benefit in reducing DBTT. Researchers have studied the role of Ta in RAFM steels and found that it stabilises the microstructure by promoting the formation of fine MX precipitates, which mitigate radiation-induced defect accumulation and

limit the formation of embrittling phases [53,54]. HRTEM observations further revealed that, after irradiation, regions containing MX precipitates exhibited a reduced size and density of dislocation loops, indicating that Ta effectively suppresses defect evolution and mitigates embrittlement [55]. Additionally, Ta influences the stability of radiation-induced precipitates such as Laves phase and $M_{23}C_6$ carbides, potentially reducing their detrimental effects on grain boundary embrittlement and dislocation mobility [56]. Notably, no significant red or orange regions appear in any temperature range, further supporting the conclusion that Ta does not contribute to embrittlement even at elevated temperatures. These findings indicate that Ta acts as a beneficial alloying element in RAFM steels by consistently improving irradiation resistance and suppressing DBTT across all temperature ranges.

Fig. 6(b) shows a polar coordinate chart of W content, revealing that DBTT decreases with increasing W content, with green regions gradually expanding even at lower temperatures, unlike in the earlier plot versions. At lower temperatures and low W concentrations (<0.5 wt. %), DBTT shows slightly elevated values (yellow zones), but no longer displays extreme red regions, indicating only moderate embrittlement.

The contour plot reveals two distinct temperature-dependent trends in the DBTT response to W content. W is a high-temperature resistant element, and in RAFM steels, it promotes the precipitation of $M_{23}C_6$ and MX carbides, where M primarily represents W, Cr, and Fe [57,58]. Studies have shown that in the 0–300 °C range, W enhances microstructural stability by forming $M_{23}C_6$ carbides, which suppress grain boundary embrittlement, thereby reducing DBTT [49,50]. However, in the 300–375 °C range, DBTT behaviour varies with W content: it is higher in low-W steels and lower in high-W steels. This trend is driven by W's effects on irradiation-induced defects, precipitate formation, and solid solution strengthening. In low-W steels, irradiation-induced vacancies and interstitial clusters tend to aggregate, increasing dislocation density and embrittlement, which raises the DBTT [59]. In high-W steels, reduced defect mobility mitigates irradiation hardening, lowering DBTT [60]. W also affects precipitate evolution. In low-W steels, limited Laves phase, Fe_2W [61], formation and increased $M_{23}C_6$ carbide precipitation at grain boundaries cause embrittlement and higher DBTT. In high-W steels, Laves phase formation is promoted while carbide coarsening is suppressed, reducing DBTT [62]. W also strengthens the solid solution and inhibits dislocation climb, improving creep resistance and irradiation stability, which further lowers DBTT in the 300–375 °C range [63].

Fig. 6(c) shows a polar coordinate chart of Cr content, revealing that DBTT increases significantly at lower Cr contents (2–4 wt. %), particularly in the 150 °C–300 °C range, where concentrated orange-red regions appear, indicating moderate to severe embrittlement. As Cr content increases beyond 6 wt. %, DBTT generally decreases, with green areas appearing at higher temperatures (>300 °C), suggesting improved toughness. However, moderate embrittlement persists at mid-range Cr levels (4–6 wt. %) and intermediate temperatures (150 °C–300 °C).

In the 0–150 °C range, DBTT remains relatively low across all Cr concentrations, similar to W, as Cr promotes the formation of $M_{23}C_6$ and MX carbides, which help maintain structural stability by hindering radiation-induced defect accumulation and suppressing grain boundary embrittlement [49,50]. Additionally, studies have shown that at low temperatures, Cr diffusion is limited, preventing excessive Cr-rich phase precipitation and minimising its impact on DBTT [18]. However, in the 150–300 °C range, DBTT increases sharply at moderate Cr concentrations (2–6 wt. %), as Cr segregation at grain boundaries intensifies due to radiation-induced segregation (RIS), promoting the formation of $M_{23}C_6$ and MX precipitates, which restrict grain boundary mobility and dislocation movement, leading to embrittlement [16,17]. At higher

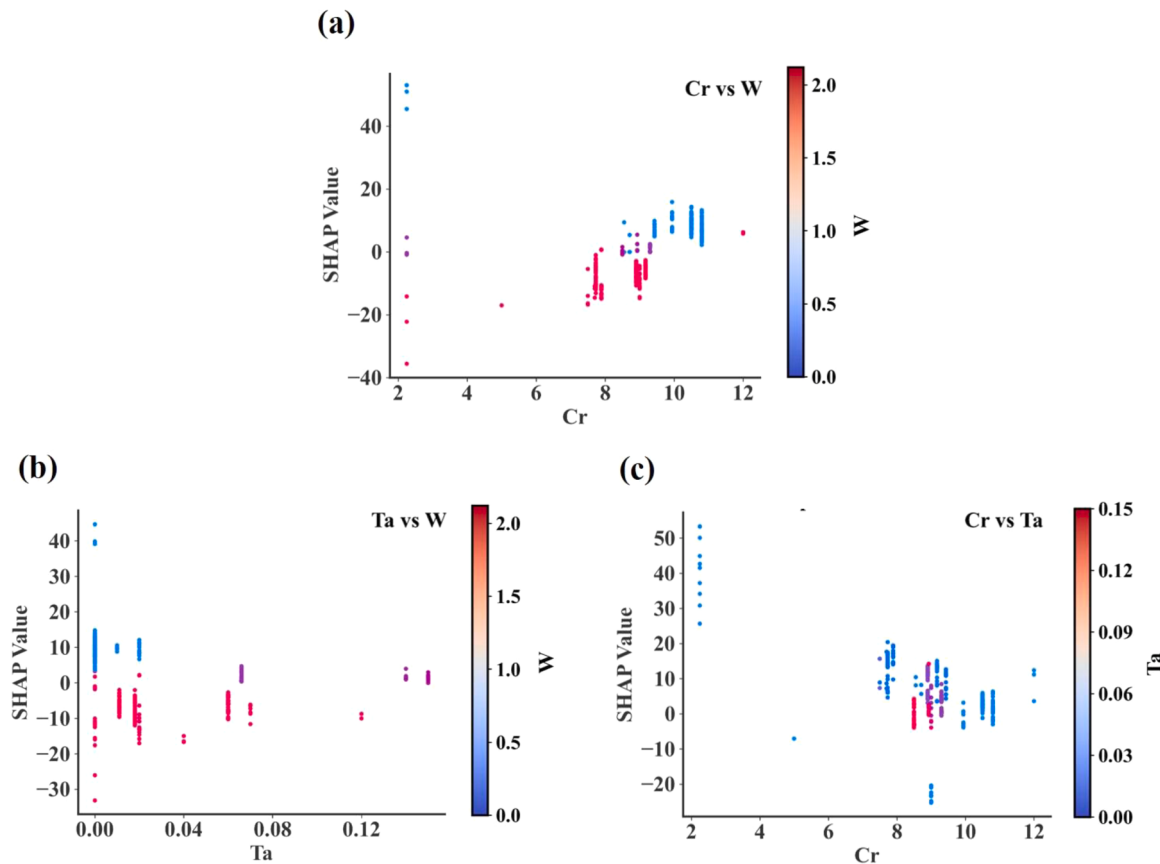


Fig. 7. SHAP Dependence Plots showing the interaction effects of alloying elements as indicated on DBTT. Each chart provides a visual representation of SHAP values, with the primary element content (wt. %), SHAP values, and the colour scale representing the interacting element content (wt. %).

temperatures (300–375 °C), DBTT continues to rise in Cr-rich regions but less significantly above 6 wt. %, likely due to precipitation saturation and the onset of vacancy-mediated Cr redistribution, which reduces grain boundary enrichment [64]. Additionally, partial defect recovery mechanisms, such as grain boundary relaxation and dislocation rearrangement, may mitigate some of the embrittlement, preventing further DBTT escalation [51].

3.5. Elemental interactions

The synergistic interactions between alloying elements are essential for optimising material composition. Understanding these interactions provides valuable insights for adjusting element concentrations to achieve desirable mechanical properties. In this study, SHAP (SHapley Additive exPlanations) dependence plots were utilised to analyse the interactions among Cr, Ta, and W, which significantly influence the ductile-to-brittle transition temperature (DBTT). Given that the predictive model is a stacking regressor incorporating multiple base models, including a Multi-Layer Perceptron (MLP), SHAP interaction values were computed separately for each base model and subsequently averaged. For tree-based models (XGBoost, GBDT, and Random Forest), TreeExplainer was employed to extract both SHAP values and interaction values. For the MLP, a neural network model, KernelExplainer was used to estimate SHAP values. To ensure consistency across models, the SHAP values from the MLP were expanded and repeated across features prior to averaging with the interaction values from the tree-based models. As illustrated in Fig. 7, the SHAP dependence plots

demonstrate the computed interactions, revealing how Cr, Ta, and W collectively influence the DBTT.

Fig. 7(a) depicts the influence of Cr and W on DBTT across different concentration ranges. Notably, when Cr = 6 ~ 9 wt. %, high W content (>1.5 wt. %) lowers DBTT, suggesting that W contributes to improved toughness in this range. The primary mechanism at play here is the solid solution strengthening effect of W [65,66], which enhances dislocation interactions while suppressing α' phase precipitation [64,67,68]. Additionally, as Cr concentration remains relatively low in this range, it does not significantly promote Laves phase formation, allowing W to primarily act as a solid solution strengthening element rather than forming embrittling precipitates [69]. Conversely, in the Cr = 9 ~ 12 wt. % range, low W content (<1.0 wt. %) increases DBTT, suggesting that insufficient W levels promote embrittlement. This may be attributed to the diminished solid solution strengthening effect. Furthermore, previous studies have reported that Cr-rich α' precipitates were not observed in 9Cr steels after irradiation but were detected in 12Cr and 13Cr steels [70,71], which is known to significantly raise DBTT. This suggests that, within the 9–12 wt. % Cr range, increasing Cr content may increase the tendency for Cr-rich α' phase formation. At high Cr concentrations (>9 wt. %), Cr may also facilitate Laves phase precipitation, which can further contribute to embrittlement [72]. In this context, higher W concentrations could mitigate these effects by promoting solid solution strengthening and stabilising the microstructure, while lower W concentrations may exacerbate them, leading to increased DBTT.

Fig. 7(b) highlights the interaction between Ta and W in influencing DBTT. Across all Ta concentrations, higher W content consistently

reduces DBTT, while lower W content increases DBTT, with this trend becoming more pronounced at lower Ta concentrations ($Ta < 0.06$). This suggests that W plays a more significant role in influencing DBTT when Ta levels are insufficient to stabilise the microstructure [53]. When W concentration is high (>1.5 wt. %), W primarily enhances solid solution strengthening, improving dislocation interactions and reducing α' phase formation [64–66]. Additionally, at low Ta concentrations, limited TaC precipitation may further accentuate the strengthening effect of W. Conversely, when W concentration is low (<1.0 wt. %), solid solution strengthening is diminished, increasing the likelihood of α' phase precipitation and raising the DBTT [72]. This indicates that at low W levels, Cr-induced α' phase formation may proceed uninhibited, thereby exacerbating radiation-induced embrittlement.

Fig. 7(c) illustrates the interaction between Cr and Ta in influencing the ductile-to-brittle transition temperature (DBTT). When both Cr and Ta concentrations are low ($Cr < 6$, $Ta < 0.06$), DBTT is at its highest, indicating increased material brittleness in this region. This effect can be attributed to the insufficient formation of carbide precipitates (such as TaC), which play a critical role in stabilising the microstructure [53]. Since both Cr and Ta contribute to carbide formation and microstructural stability, their absence may allow uncontrolled microstructural evolution, promoting embrittlement through mechanisms [7,22,54,55]. As Cr content exceeds 6 wt. %, DBTT exhibits minimal variation regardless of Ta content, indicating that Cr dominates microstructural stability while Ta has a limited effect. In this range, Cr effectively prevents α' phase precipitation and enhances solid solution strengthening, thereby maintaining a relatively stable DBTT [67,68,72]. This suggests that above a threshold level of Cr (>6 wt. %), its strengthening effect is sufficient to stabilise the microstructure, reducing the relative impact of Ta on DBTT.

3.6. Optimising RAFM compositions

To identify steel compositions with enhanced resistance to irradiation-induced embrittlement, a genetic algorithm (GA) was employed in combination with the trained stacking ensemble model to minimise the predicted ductile-to-brittle transition temperature (DBTT). The GA was implemented using the DEAP framework, with a population size of 100 evolved over 120 generations. Blend crossover ($\alpha = 0.5$) and Gaussian mutation ($\sigma = 0.1$, mutation probability = 0.4) were applied, together with tournament selection (size = 3). The ten best-performing individuals were retained through a Hall of Fame strategy.

The optimisation was conducted under realistic service conditions, with T_{irr} constrained to 250–350 °C, which corresponds to the embrittlement-dominated regime observed in RAFM steels, as clearly illustrated in Fig. 5. The irradiation dose was fixed at 10 dpa, a representative mid-dose level that lies within the range of available experimental data and coincides with the transition region where DBTT tends to increase sharply. Moreover, this value is well represented in the training dataset, ensuring reliable model predictions during optimisation. The DBTT was constrained to the range of –50 to +50 °C, which is generally considered acceptable for avoiding brittle failure in structural applications.

To ensure physical feasibility and nuclear compatibility, the composition search space excluded high activation elements such as Ni, Co and Mo [41,73], which were fixed to zero. All other alloying elements were allowed to vary within physically meaningful ranges to ensure metallurgical feasibility and maintain low-activation characteristics. This ensures that the generated compositions meet irradiation tolerance targets and comply with reduced-activation criteria.

The optimisation yielded a set of candidate compositions that meet all constraints and achieve low predicted DBTT values. Two representative solutions, presented in Table 1, demonstrate the effectiveness of the proposed approach and offer practical guidance for the design of irradiation-tolerant RAFM steels.

Table 1

Optimised RAFM steel compositions (wt. %) using a genetic algorithm based on a radiation embrittlement prediction model.

Alloy	C	Si	Mn	Cr	W	Ta	V	Fe
1	0.09	0.35	0.54	8.28	2.97	0.14	0.22	Bal.
2	0.14	0.33	0.67	9.18	4.5	0.08	0.27	Bal.

4. Conclusion

This study developed a stacking ensemble machine learning model to predict the DBTT in irradiated reduced-activation ferritic/martensitic (RAFM) steels. By integrating XGBoost, Random Forest, GBDT, and MLP models, the ensemble achieved high predictive accuracy ($R^2 = 0.96$), significantly outperforming individual models. The stacking framework effectively mitigates overfitting and enhances generalisation, making it a robust tool for analysing radiation-induced embrittlement trends. The results demonstrate a strong dependency of DBTT on both irradiation dose and temperature. Specifically, DBTT increases markedly beyond 30 dpa due to defect accumulation, dislocation pinning, and precipitation evolution. A nonlinear temperature response was observed, with DBTT rising between 150 and 300 °C owing to radiation-enhanced segregation and the precipitation of $M_{23}C_6$, MX, and Laves phases. However, temperatures above 350 °C promote defect recovery and grain boundary relaxation, leading to a reduction in DBTT and an improvement in ductility. The effects of alloying elements were systematically explored, revealing that tantalum reduces embrittlement by stabilising MX precipitates and suppressing defect build-up. Tungsten improves radiation resistance at high doses (>40 dpa) by enhancing microstructural stability, while chromium exhibits a dual effect: moderate levels (4–6 wt. %) increase DBTT due to radiation-induced segregation, whereas higher concentrations (>6 wt. %) lower DBTT at elevated temperatures via defect redistribution and carbide stabilisation. SHAP analysis further elucidated these interactions, showing that tungsten reduces DBTT through solid solution strengthening, particularly at moderate chromium (6–9 wt. %) and low tantalum content. Chromium's dual role was reaffirmed, with low Cr and Ta levels leading to increased DBTT, while higher Cr (>6 wt. %) contributes to stabilisation by controlling microstructural evolution. Based on these insights, a genetic algorithm was applied to optimise chemical compositions under defined irradiation conditions. The resulting alloys satisfied key constraints on temperature, dose, and embrittlement, demonstrating the model's capability to predict DBTT and to guide practical alloy design. Collectively, these findings provide valuable insights into the complex interplay between composition, irradiation conditions, and embrittlement, underscoring the transformative potential of machine learning as a computationally efficient approach for predicting and mitigating irradiation-induced embrittlement in RAFM steels.

Data availability

The data supporting this study are included with the manuscript but require prior permission for use.

CRediT authorship contribution statement

Pengxin Wang: Writing – original draft, Validation, Software, Methodology, Investigation, Funding acquisition, Data curation, Conceptualization. **G.M.A.M. El-Fallah:** Writing – review & editing, Visualization, Validation, Supervision, Software, Methodology, Investigation, Formal analysis, Data curation, Conceptualization.

Declaration of competing interest

The authors declare that they have no known competing financial interests or personal relationships that could have appeared to influence

the work reported in this paper.

Acknowledgements

All authors gratefully acknowledge the support from Nanjing Iron & Steel United Co., Ltd. (NISCO), particularly for providing a PhD. Scholarship for this study.

Supplementary materials

Supplementary material associated with this article can be found, in the online version, at [doi:10.1016/j.jnucmat.2025.155984](https://doi.org/10.1016/j.jnucmat.2025.155984).

References

- [1] N. Baluc, et al., Status of reduced activation ferritic/martensitic steel development, *J. Nucl. Mater.* 367-370 (2007) 33–41, <https://doi.org/10.1016/j.jnucmat.2007.03.036>.
- [2] A. Bhattacharya, et al., Irradiation hardening and ductility loss of Eurofer97 steel variants after neutron irradiation to ITER-TBM relevant conditions, *Fusion Eng. Des.* (2021) 173, <https://doi.org/10.1016/j.fusengdes.2021.112935>.
- [3] O. Anderoglu, et al., Mechanical performance of ferritic martensitic steels for high dose applications in advanced nuclear reactors, *Metallurg. Mater. Trans. A* 44 (2012) 70–83, <https://doi.org/10.1007/s11661-012-1565-y>.
- [4] C. Cabet, et al., Ferritic-martensitic steels for fission and fusion applications, *J. Nucl. Mater.* 523 (2019) 510–537, <https://doi.org/10.1016/j.jnucmat.2019.05.058>.
- [5] E. Gaganidze, et al., Mechanical properties and TEM examination of RAFM steels irradiated up to 70dpa in BOR-60, *J. Nucl. Mater.* 417 (2011) 93–98, <https://doi.org/10.1016/j.jnucmat.2010.12.047>.
- [6] M. Rieth, et al., Technological aspects in blanket design: effects of micro-alloying and thermo-mechanical treatments of EUROFER97 type steels after neutron irradiation, *Fusion Eng. Des.* (2021) 168, <https://doi.org/10.1016/j.fusengdes.2021.112645>.
- [7] S. Rogozhkin, et al., Evolution of microstructure in advanced ferritic-martensitic steels under irradiation: the origin of low temperature radiation embrittlement, *MRS Adv* 2 (2016) 1143–1155, <https://doi.org/10.1557/adv.2016.657>.
- [8] J. Knaster, A. Moeslang, T. Muroga, Materials research for fusion, *Nat. Phys.* 12 (2016) 424–434, <https://doi.org/10.1038/nphys3735>.
- [9] Y. Dai, et al., Neutron/proton irradiation and He effects on the microstructure and mechanical properties of ferritic/martensitic steels T91 and EM10, *J. Nucl. Mater.* 415 (2011) 306–310, <https://doi.org/10.1016/j.jnucmat.2011.04.029>.
- [10] M. Kiritani, Defect structure evolution from radiation damage with D-T fusion neutrons, *J. Nucl. Mater.* 133–134 (1985) 85–91, [https://doi.org/10.1016/0022-3115\(85\)90116-3](https://doi.org/10.1016/0022-3115(85)90116-3).
- [11] T. Zhang, et al., Irradiation-induced evolution of mechanical properties and microstructure of Eurofer 97, *J. Nucl. Mater.* 450 (2014) 48–53, <https://doi.org/10.1016/j.jnucmat.2013.12.007>.
- [12] R.L. Klueh, K. Shiba, M.A. Sokolov, Embrittlement of irradiated ferritic/martensitic steels in the absence of irradiation hardening, *J. Nucl. Mater.* 377 (2008) 427–437, <https://doi.org/10.1016/j.jnucmat.2008.04.002>.
- [13] S.H. Song, et al., Small punch test evaluation of neutron-irradiation-induced embrittlement of a Cr-Mo low-alloy steel, *Mater. Charact.* 53 (2004) 35–41, <https://doi.org/10.1016/j.matchar.2004.07.006>.
- [14] S.H. Song, et al., Irradiation-induced embrittlement of a 2.25Cr1Mo steel, *J. Nucl. Mater.* 280 (2000) 162–168, [https://doi.org/10.1016/S0022-3115\(00\)00042-8](https://doi.org/10.1016/S0022-3115(00)00042-8).
- [15] Y. Nishiyama, et al., Effects of neutron-irradiation-induced intergranular phosphorus segregation and hardening on embrittlement in reactor pressure vessel steels, *Acta Mater.* 56 (2008) 4510–4521, <https://doi.org/10.1016/j.actamat.2008.05.026>.
- [16] D. Terentev, A. Bakaev, Radiation-induced strengthening and absorption of dislocation loops in ferritic Fe-Cr alloys: the role of Cr segregation, *J. Phys. Condens Matter* 25 (2013) 265702, <https://doi.org/10.1088/0953-8984/25/26/265702>.
- [17] Z. Jiao, G.S. Was, Segregation behavior in proton- and heavy-ion-irradiated ferritic-martensitic alloys, *Acta Mater.* 59 (2011) 4467–4481, <https://doi.org/10.1016/j.actamat.2011.03.070>.
- [18] L.D. Xia, et al., Radiation induced grain boundary segregation in ferritic/martensitic steels, *Nucl. Eng. Technol.* 52 (2020) 148–154, <https://doi.org/10.1016/j.net.2019.07.009>.
- [19] H. Tanigawa, et al., Irradiation effects on precipitation and its impact on the mechanical properties of reduced-activation ferritic/martensitic steels, *J. Nucl. Mater.* 367–370 (2007) 42–47, <https://doi.org/10.1016/j.jnucmat.2007.03.167>.
- [20] L. Tan, et al., Recent status and improvement of reduced-activation ferritic-martensitic steels for high-temperature service, *J. Nucl. Mater.* 479 (2016) 515–523, <https://doi.org/10.1016/j.jnucmat.2016.07.054>.
- [21] R. Coppola, M. Klimenkov, Dose dependence of micro-voids distributions in low-temperature neutron irradiated Eurofer97 steel, *Metals* 9 (2019), <https://doi.org/10.3390/met9050552>.
- [22] M. Johnson, et al., Irradiation-induced microstructure and microchemistry effects on mechanical properties in ferritic-martensitic alloys, *Materialia* 20 (2021), <https://doi.org/10.1016/j.mtla.2021.101228>.
- [23] V. Kuksenko, et al., Effect of neutron-irradiation on the microstructure of a Fe-12at.%Cr alloy, *J. Nucl. Mater.* 415 (2011) 61–66, <https://doi.org/10.1016/j.jnucmat.2011.05.042>.
- [24] S.J. Zinkle, et al., Fusion materials science and technology research opportunities now and during the ITER era, *Fusion Eng. Des.* 89 (2014) 1579–1585, <https://doi.org/10.1016/j.fusengdes.2014.02.048>.
- [25] A.A.F. Tavassoli, et al., Current status and recent research achievements in ferritic/martensitic steels, *J. Nucl. Mater.* 455 (2014) 269–276, <https://doi.org/10.1016/j.jnucmat.2014.06.017>.
- [26] B.-S. Lee, et al., Master curve techniques to evaluate an irradiation embrittlement of nuclear reactor pressure vessels for a long-term operation, *Int. J. Press. Vessels Pip.* 85 (2008) 593–599, <https://doi.org/10.1016/j.ijpvp.2007.08.005>.
- [27] R. Moskovic, et al., A bayesian analysis of the influence of neutron irradiation on embrittlement in ferritic submerged arc weld metal, *Metallurg. Mater. Trans. A* 31 (2000) 445–459, <https://doi.org/10.1007/s11661-000-0281-1>.
- [28] S. Kotrechko, Y. Meshkov, A new approach to estimate irradiation embrittlement of pressure vessel steels, *Int. J. Press. Vessels Pip.* 85 (2008) 336–343, <https://doi.org/10.1016/j.ijpvp.2007.10.012>.
- [29] Y. Zou, et al., Machine learning-assisted prediction and interpretation of electrochemical corrosion behavior in high-entropy alloys, *Comput. Mater. Sci.* 244 (2024) 113259, <https://doi.org/10.1016/j.commatsci.2024.113259>.
- [30] C. Herriott, A.D. Spear, Predicting microstructure-dependent mechanical properties in additively manufactured metals with machine- and deep-learning methods, *Comput. Mater. Sci.* 175 (2020) 109599, <https://doi.org/10.1016/j.commatsci.2020.109599>.
- [31] X. Huang, et al., Study on time-temperature-transformation diagrams of stainless steel using machine-learning approach, *Comput. Mater. Sci.* 171 (2020) 109282, <https://doi.org/10.1016/j.commatsci.2019.109282>.
- [32] P. Wang, et al., Advanced machine learning analysis of radiation hardening in reduced-activation ferritic/martensitic steels, *Comput. Mater. Sci.* 251 (2025) 113773, <https://doi.org/10.1016/j.commatsci.2025.113773>.
- [33] P. Korotaev, A. Yanilkin, Neural networks for prediction of swelling in austenitic steels irradiated by fast neutrons, *Comput. Mater. Sci.* 246 (2025), <https://doi.org/10.1016/j.commatsci.2024.113408>.
- [34] L. Johnson, et al., Machine learning method to determine concentrations of structural defects in irradiated materials, *Comput. Mater. Sci.* 242 (2024), <https://doi.org/10.1016/j.commatsci.2024.113079>.
- [35] B. Zhu, et al., Machine learning powered predictive modelling of complex residual stress for nuclear fusion reactor design, *Mater. Des.* 248 (2024), <https://doi.org/10.1016/j.matdes.2024.113449>.
- [36] W.-K. He, et al., Study on irradiation embrittlement behavior of reactor pressure vessels by machine learning methods, *Ann. Nucl. Energy* 192 (2023), <https://doi.org/10.1016/j.anucene.2023.109965>.
- [37] G.-G. Lee, M.-C. Kim, B.-S. Lee, Machine learning modeling of irradiation embrittlement in low alloy steel of nuclear power plants, *Nucl. Eng. Technol.* 53 (2021) 4022–4032, <https://doi.org/10.1016/j.net.2021.06.014>.
- [38] C. Xu, et al., A study of predicting irradiation-induced transition temperature shift for RPV steels with XGBoost modeling, *Nucl. Eng. Technol.* 53 (2021) 2610–2615, <https://doi.org/10.1016/j.net.2021.02.015>.
- [39] R. Jacobs, et al., Predictions and uncertainty estimates of reactor pressure vessel steel embrittlement using machine learning, *Mater. Des.* 236 (2023), <https://doi.org/10.1016/j.matdes.2023.112491>.
- [40] G.J. Butterworth, Low activation structural materials for fusion, *Fusion Eng. Des.* 11 (1989) 231–244, [https://doi.org/10.1016/0920-3796\(89\)90021-5](https://doi.org/10.1016/0920-3796(89)90021-5).
- [41] T. Noda, et al., Materials selection for reduced activation of fusion reactors, *J. Nucl. Mater.* 155–157 (1988) 581–584, [https://doi.org/10.1016/0022-3115\(88\)90375-3](https://doi.org/10.1016/0022-3115(88)90375-3).
- [42] J. Rensman, et al., Characteristics of unirradiated and 60 C, 2.7 dpa irradiated Eurofer97, *J. Nucl. Mater.* 307 (2002) 250–255, [https://doi.org/10.1016/S0022-3115\(02\)01036-X](https://doi.org/10.1016/S0022-3115(02)01036-X).
- [43] K. Shiba, A. Hishinuma, Low-temperature irradiation effects on tensile and charpy properties of low-activation ferritic steels, *J. Nucl. Mater.* 283–287 (2000) 474–477, [https://doi.org/10.1016/S0022-3115\(00\)00369-X](https://doi.org/10.1016/S0022-3115(00)00369-X).
- [44] X. Jia, Y. Dai, Small punch tests on martensitic/ferritic steels F82H, T91 and Optimax-A irradiated in SINQ Target-3, *J. Nucl. Mater.* 323 (2003) 360–367, <https://doi.org/10.1016/j.jnucmat.2003.08.018>.
- [45] M. Kolluri, et al., A structure-property correlation study of neutron irradiation induced damage in EU batch of ODS Eurofer97 steel, *Mater. Sci. Eng. A* 597 (2014) 111–116, <https://doi.org/10.1016/j.msea.2013.12.074>.
- [46] Y. Zheng, et al., Variation of radiation damage with irradiation temperature and dose in CLAM steel, *Plasma Sci. Technol.* 14 (2012) 629–631, <https://doi.org/10.1088/1009-0630/14/7/14>.
- [47] C. Zheng, et al., Microstructure response of ferritic/martensitic steel HT9 after neutron irradiation effect of dose, *J. Nucl. Mater.* 523 (2019) 421–433, <https://doi.org/10.1016/j.jnucmat.2019.06.019>.
- [48] R. Kasada, et al., Effects of varying temperature irradiation on the neutron irradiation hardening of reduced-activation 9Cr-2W martensitic steels, *J. Nucl. Mater.* 271–272 (1999) 360–364, [https://doi.org/10.1016/S0022-3115\(98\)00749-1](https://doi.org/10.1016/S0022-3115(98)00749-1).
- [49] X. Jia, Y. Dai, M. Victoria, The impact of irradiation temperature on the microstructure of F82H martensitic/ferritic steel irradiated in a proton and neutron mixed spectrum, *J. Nucl. Mater.* 305 (2002) 1–7, [https://doi.org/10.1016/S0022-3115\(02\)00916-9](https://doi.org/10.1016/S0022-3115(02)00916-9).
- [50] X. Jia, Y. Dai, Microstructure in martensitic steels T91 and F82H after irradiation in SINQ Target-3, *J. Nucl. Mater.* 318 (2003) 207–214, [https://doi.org/10.1016/S0022-3115\(03\)00101-6](https://doi.org/10.1016/S0022-3115(03)00101-6).

- [51] E. Materna-Morris, et al., Effect of helium on tensile properties and microstructure in 9%Cr-WVTA-steel after neutron irradiation up to 15dpa between 250 and 450°C, *J. Nucl. Mater.* 386–388 (2009) 422–425, <https://doi.org/10.1016/j.jnucmat.2008.12.157>.
- [52] M. Klimenkov, et al., Correlation of microstructural and mechanical properties of neutron irradiated EUROFER97 steel, *J. Nucl. Mater.* (2020) 538, <https://doi.org/10.1016/j.jnucmat.2020.152231>.
- [53] X. Xiao, et al., Effect of V and Ta on the precipitation behavior of 12 %Cr reduced activation ferrite/martensite steel, *Mater. Charact.* 82 (2013) 130–139, <https://doi.org/10.1016/j.matchar.2013.05.006>.
- [54] X. Xiao, et al., Microstructure stability of V and Ta microalloyed 12 %Cr reduced activation ferrite/martensite steel during long-term aging at 650°C, *J. Mater. Sci. Technol.* 31 (2015) 311–319, <https://doi.org/10.1016/j.jmst.2013.04.028>.
- [55] P.P. Liu, et al., Effects of carbide precipitate on the mechanical properties and irradiation behavior of the low activation martensitic steel, *J. Alloys Compd.* 579 (2013) 599–605, <https://doi.org/10.1016/j.jallcom.2013.07.085>.
- [56] L. Tan, W. Zhong, and T. Chen, Microstructural stability of tantalum-alloyed ferritic-martensitic steel with neutron irradiation to 7.4 dpa at ~490 °C, *Materialia*, 9 (2020), <https://doi.org/10.1016/j.mtla.2020.100608>.
- [57] P. Fernández, et al., Creep strength of reduced activation ferritic/martensitic steel Eurofer'97, *Fusion Eng. Des.* 75–79 (2005) 1003–1008, <https://doi.org/10.1016/j.fusengdes.2005.06.085>.
- [58] S. Yin, et al., Stabilities of the precipitates in CLAM steel during 30,000 h thermal aging, *J. Nucl. Mater.* 567 (2022) 153805, <https://doi.org/10.1016/j.jnucmat.2022.153805>.
- [59] R.O. Kaybyshev, V.N. Skorobogatykh, I.A. Shchenkova, New martensitic steels for fossil power plant: creep resistance, *Phys. Metals Metallogr.* 109 (2010) 186–200, <https://doi.org/10.1134/s0031918x10020110>.
- [60] F. Abe, Effect of fine precipitation and subsequent coarsening of Fe2W laves phase on the creep deformation behavior of tempered martensitic 9Cr-W steels, *Metallurg. Mater. Trans. A* 36 (2005) 321–332, <https://doi.org/10.1007/s11661-005-0305-y>.
- [61] C. Mao, et al., Revealing the stabilization mechanism of coupling effect of Ta/Zr on M23C6 and laves precipitations in low-carbon 9Cr ferrite/martensite (F/M) steels: experiment and ab initio molecular dynamics, *Metallurg. Mater. Trans. A* 55 (2024) 5070–5089, <https://doi.org/10.1007/s11661-024-07599-y>.
- [62] M. Taneike, K. Sawada, F. Abe, Effect of carbon concentration on precipitation behavior of M23C6 carbides and MX carbonitrides in martensitic 9Cr steel during heat treatment, *Metallurg. Mater. Trans. A* 35 (2004) 1255–1262, <https://doi.org/10.1007/s11661-004-0299-x>.
- [63] P.J. Ennis, A. Cyrska-Filemonowicz, Recent advances in creep-resistant steels for power plant applications, *Sadhana* 28 (2003) 709–730, <https://doi.org/10.1007/BF02706455>.
- [64] M.J. Konstantinović, et al., Mechanical and microstructural properties of neutron irradiated Fe-Cr-C alloys, *Phys. Status Solidi (a)* 213 (2016) 2988–2994, <https://doi.org/10.1002/pssa.201600316>.
- [65] A. Pupye, et al., Effect of W and N on mechanical properties of reduced activation ferritic/martensitic EUROFER-based steel grades, *J. Nucl. Mater.* 502 (2018) 282–288, <https://doi.org/10.1016/j.jnucmat.2018.02.017>.
- [66] R. Kirana, et al., High-temperature phase stability of 9Cr-W-Ta-V-C based reduced activation ferritic-Martensitic (RAFM) steels: effect of W and Ta additions, *Steel Res. Int.* 86 (2015) 825–840, <https://doi.org/10.1002/srin.201400183>.
- [67] A. Alamo, et al., Assessment of ODS-14 %Cr ferritic alloy for high temperature applications, *J. Nucl. Mater.* 329–333 (2004) 333–337, <https://doi.org/10.1016/j.jnucmat.2004.05.004>.
- [68] H.S. Cho, R. Kasada, A. Kimura, Effects of neutron irradiation on the tensile properties of high-Cr oxide dispersion strengthened ferritic steels, *J. Nucl. Mater.* 367–370 (2007) 239–243, <https://doi.org/10.1016/j.jnucmat.2007.03.140>.
- [69] F.A. Garner, Influence of radiation on material properties: 13th International Symposium (part II): a Symposium sponsored by ASTM Committee E-10 on Nuclear Technology and Applications, Seattle, WA, 23–25, June 1986, in: C.H.H. F. A. Garner, Naohiro Igata (Ed.), ASTM International, New York, 1987, pp. 501–523.
- [70] Y.I. Zvezdin, et al., Radiation embrittlement and recovery annealing regularities of ITER blanket 9Cr steel, *J. Nucl. Mater.* 191–194 (1992) 855–857, [https://doi.org/10.1016/0022-3115\(92\)90594-B](https://doi.org/10.1016/0022-3115(92)90594-B).
- [71] O.V. Borodin, et al., Investigation of microstructure of ferritic-martensitic steels containing 9 and 13 % Cr irradiated with fast neutrons, *J. Nucl. Mater.* 207 (1993) 295–302, [https://doi.org/10.1016/0022-3115\(93\)90272-Z](https://doi.org/10.1016/0022-3115(93)90272-Z).
- [72] F.A. Garner, Influence of radiation on material properties: 13th International Symposium (part II): a Symposium sponsored by ASTM Committee E-10 on Nuclear Technology and Applications, Seattle, WA, 23–25, June 1986, in: C.H.H. F. A. Garner, Naohiro Igata (Ed.), ASTM International, New York, 1987, pp. 216–331.
- [73] G.J. Butterworth and P. Komarek, LOW ACTIVATION STRUCTURAL MATERIALS FOR FUSION **A version of this paper was presented as an invited paper at the 15th Symposium on Fusion Technology, held in Utrecht, The Netherlands, September 19–23, 1988, in: A.M. Van Ingen, A. Nijsen-Vis, and H.T. Klippen (Ed.), *Fusion Technology* 1988, Elsevier, Oxford, 1989, pp. 231–244.